ELSEVIER

Coordination Chemistry Reviews
174 (1998) 361–390

COORDINATION CHEMISTRY REVIEWS

Designing ligands to achieve robust oxidation catalysts. Iron based systems

Michael J. Bartos [a], Scott W. Gordon-Wylie [a], Brian G. Fox [a], L. James Wright [a], Susan T. Weintraub [b], Karl E. Kauffmann [a], Eckard Münck [a,*], Kimberly L. Kostka [a], Erich S. Uffelman [a], Clifton E. F. Rickard [c], Kathleen R. Noon [d], Terrence J. Collins [a,*]

[a] *Department of Chemistry, Carnegie Mellon University, 4400 Fifth Avenue, Pittsburgh, PA 15213, USA*
[b] *Department of Pathology, Graduate School of Biomedical Sciences, University of Texas Health Sciences Center, San Antonio, TX 78284, USA*
[c] *Department of Chemistry, University of Auckland, Private Bag 92019, Auckland, New Zealand*
[d] *Department of Chemistry, Michigan State University, East Lansing, MI 48824, USA*

Received 27 October 1997; accepted 26 May 1998

Contents

* Corresponding author. Tel: +1 412 268 3125; Fax: +1 412 268 1061; E-mail: tclu@andrew.cmu.edu

PII S0010-8545(98)00142-8

Abstract

Nitrile solvents containing α-CH substituents are catalytically oxidized by the tetraamido-*N*-Fe^{III}-aqua complex, **3**, with *t*-butyl hydroperoxide. Every observable product resulting from **3** has been characterized. An Fe^{IV}–cyano complex, **5**, is the major inorganic product; the cyano ligand emanates from the solvent–substrate. A new type of ligand oxidative degradation giving **6** proceeds to ca. 10% of the iron macrocycle; its characterization indicates how the already robust macrocycle should be redesigned to further improve its oxidative stability. Such improvement has led to long-lived catalysts for hydrogen peroxide oxidation in water from neutral to basic pH at room temperature.

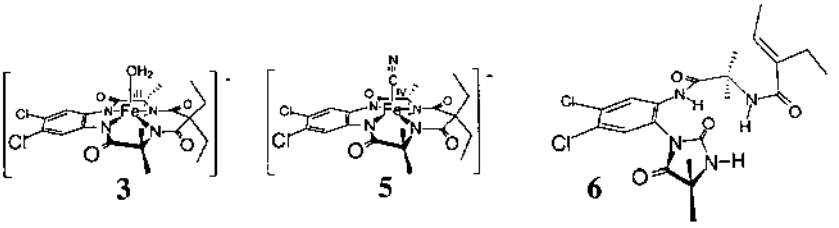

Keywords: High valent iron complexes; Iron-57 Mössbauer spectroscopy; Ligand design; Ligand oxidative degradation

1. Introduction

It is a pleasure and a privilege to be able to contribute to a *Coordination Chemistry Reviews* volume honoring Daryle Busch, a father-figure of the field of macrocyclic coordination chemistry and a statesman of inorganic chemistry. The study reported here involves the exploration of the design of iron macrocycles for use in oxidation chemistry, an area Professor Busch himself has long been interested in. More generally, there is widespread interest in the mechanisms of action of iron monooxygenase enzymes that catalyze difficult oxidations important to both biology and chemistry [1–6]. Considerable effort is devoted to the design or discovery of small molecule catalysts that might emulate monooxygenase catalysis [7–12]. Complexity is often a signature of oxidation catalysis involving potent reactive intermediates. For example, it is especially difficult to distinguish among the roles of free radical and metal-based oxidants [13–18] and it is generally difficult to design catalysts that

do not rapidly degrade [19]. In a monooxygenase enzyme, competition from protein and prosthetic group degradations is controlled by an intricate chaperoning of the reactivity down the desired channel. Thus, achieving monooxygenase reactivity in small molecule catalysts is especially difficult if one is to follow Nature's strategy of speeding up the targeted reaction, because the potent oxidizing properties required conspire against elaborate design.

A more pragmatic approach for mimicking monooxygenases lies with developing an alternative strategy, one which has as its central focus the goal of decelerating processes that might compete with a targeted oxidation [19]. Especially when potent oxidants are involved, gaining control over the selectivity of an oxidation system towards substrates requires that control also must be attained over oxidative degradation of the solvent, the primary oxidant, and the catalyst. Among these challenges, it is our belief that the most limiting has been catalyst degradation, more specifically the tendency of potential catalyst ligands to undergo oxidative degradation leading to catalyst deactivation. Thus, we have focused on developing ligands that are resistant to oxidative destruction [19]. The approach for obtaining such ligands can be summarized as follows: (1) a ligand system is designed that is thought will lead to oxidatively and hydrolytically robust complexes; (2) a metallocomplex of this ligand is produced and oxidized until ligand decay occurs; (3) the ligand degradation byproducts are fully identified, thereby revealing the ligand site that is vulnerable to oxidation; (4) the reactive group is replaced with a substitute expected to be more inert; and (5) steps 1 through 4 are repeated until complexes are obtained that are sufficiently resistant to oxidative degradation to serve in desired catalytic roles. In iron chemistry, these efforts have provided a series of stable high valent complexes and their precursors, thereby permitting studies of these rare species by Mössbauer, EPR, X-ray crystallographic, NMR, IR, electrochemical, magnetochemical and mass spectrometric methods [20–22]. Here we report on a significant step in the aforementioned design loop that provides the foundation for obtaining long-lived iron catalysts for technologically useful oxidations with hydrogen peroxide.

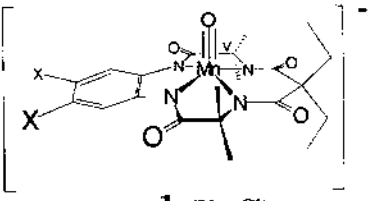

1 (X = Cl)

Several years ago we reported that Mn^{III} complexes of strongly-donating, oxidation-resistant macrocyclic tetraamides react with alkyl hydroperoxides such as *t*-butyl hydroperoxide (TBHP) to yield stable anionic Mn^{V}–oxo complexes such as **1** [23,24]. Manganyl complexes of related acyclic ligands have been produced employing alkyl hydroperoxides [25] or oxygen [26] as the oxidant. The successful synthesis of stable manganyl species led us to ask if stable Fe-analogues could be generated. This report consists of what was discovered in exploring this question. It begins

with a presentation of the structures and spectroscopy of iron complexes involved in or pertinent to the chemistry of Fe^{III}-macrocyclic tetraamides with TBHP in nitrile solvents. The reaction system produces catalytic oxidation of the nitrile solvent–substrates. Particular emphasis is given to a discussion of the characterization and origin of a minor product that arises from oxidative degradation of the macrocyclic ligand. From this identification, it is possible to proceed around the above design loop to peroxide activating iron catalysts with technologically useful lifetimes.

2. Fe(III) and Fe(IV) compounds

2.1. Synthetic pathways

Synthetic pathways to the complexes studied are presented in Scheme 1. The Fe^{III}-aqua complex, $[Et_4N]$**3** was the principal starting material for the **3**–nitrile–TBHP reactions. It was prepared from the Fe^{III}–chloro complex $[Et_4N]_2$**2**, by removal of the axial chloro ligand with a stoichiometric amount of silver(I) ion. Under these conditions ligand exchange was the observed reaction channel.

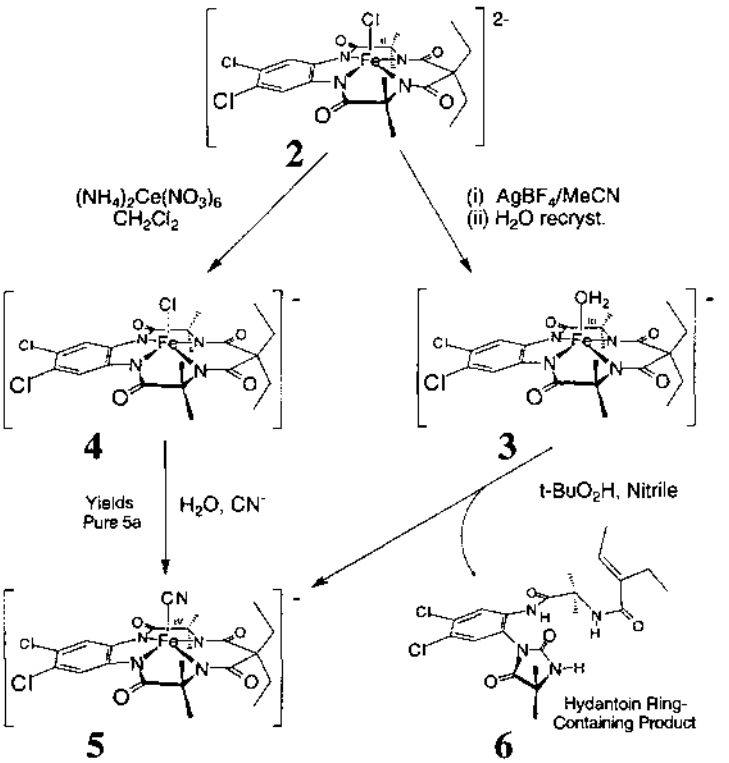

Scheme 1. Syntheses of the iron complexes employed for this study.

Compounds **2** and **3** are not oxidized by the silver(I) ion. In a closely related system with methoxy substituents in place of the aromatic chloride groups of **2**, Ag^+ is found to oxidize the Fe^{III}-aqua complex, **7**, to the neutral molecule, **8** [20]. The cyclic voltammogram of $[Et_4N]_2$**2** in CH_2Cl_2 shows a reversible oxidation wave for formation of the one-electron oxidized Fe–chloro species, **4** (+0.547 V versus SSCE). Electrochemical reduction of $[Et_4N]_2$**2** is irreversible. Chemical oxidation of $[Et_4N]_2$**2** with $Ce^{IV}(NH_3)_2(NO_3)_6$ yields $[Et_4N]$**4**, an important starting material for the independent preparation of the Fe^{IV}–cyano complex, **5**.

An understanding of the stability of **3** as a catalyst in the **3**–nitrile–TBHP system has emerged only after identification of both major and minor metal–ligand products. The major (ca. 90%) product of the **3**–nitrile–TBHP system was the Fe^{IV} cyano complex, **5**, while the minor (ca. 10%) product was identified as the hydantoin containing ligand degradation product, **6**. The inorganic synthetic processes of Scheme 1 can be easily monitored by the characteristic electronic absorptions of the different metal centred chromophores, UV–vis spectra for complexes **2**–**5** are shown in Fig. 1.

2.2. *X-ray studies*

The X-ray crystal structure for the ferric $[Et_4N]$**3**$\cdot H_2O$ complex reveals a five-coordinate square-pyramidal geometry with an axial aqua ligand (Fig. 2) and with an additional lattice water. The four ligand N-atoms are nearly planar (mean deviation from the N4 plane is 0.013 Å, with a maximum of 0.015(3) Å for N1). The Fe atom lies 0.338(3) Å above the N4-plane, but the positions of the aqua ligand H-atoms could not be located with sufficient certainty for presentation. In a recent structural study of a related Fe–aqua complex, **8**, the aqua H-atoms could be clearly located [20]. Comparison of the two structures is appropriate since both have identical immediate coordination spheres. Both **3** and **8** are Fe^{III} compounds. Compound **8** is oxidized by one electron compared to $[Et_4N]$**3**, but it has been demonstrated by Mössbauer spectroscopy, crystallography and other techniques that the site of oxidation in **8** is the diamidodimethoxyphenylene ligand group [20]. The average Fe–*N* distance is 1.875 Å in $[Et_4N]$**3** and 1.879 Å in **8**. The Fe–O distance in **8** is 2.068(3) Å and in **3** it is 2.122(7) Å indicating an expected weaker axial ligation for the latter reduced Fe^{III} complex. The diamidodimethoxyphenylene group of **8** shows significant distortions and a short average C–N distance (1.365 Å) consistent with a ligand-localized oxidation, whereas the more symmetric bond distances in the aromatic ring of the diamidodichlorophenylene group of $[Et_4N]$**3**$\cdot H_2O$ and the comparatively long average C–N distance (1.405 Å) are consistent with a non-oxidized ligand formulation [20,27].

An X-ray study also has been performed on $S=1$, $[Et_4N]$**4**$\cdot H_2O$ (Fig. 3). This compound is oxidized by one electron compared with $[Et_4N]$**3**, and has an axial chloro ligand in place of the aqua ligand. The average Fe–N distance in $[Et_4N]$**4**$\cdot H_2O$ is 1.869 Å. The four N-atoms are again nearly planar (the maximum displacement from the mean plane is 0.04 Å) with the Fe atom lying 0.16 Å above the N4-plane. The Fe–Cl distance is 2.203(1) Å. The diamidodichlorophenylene

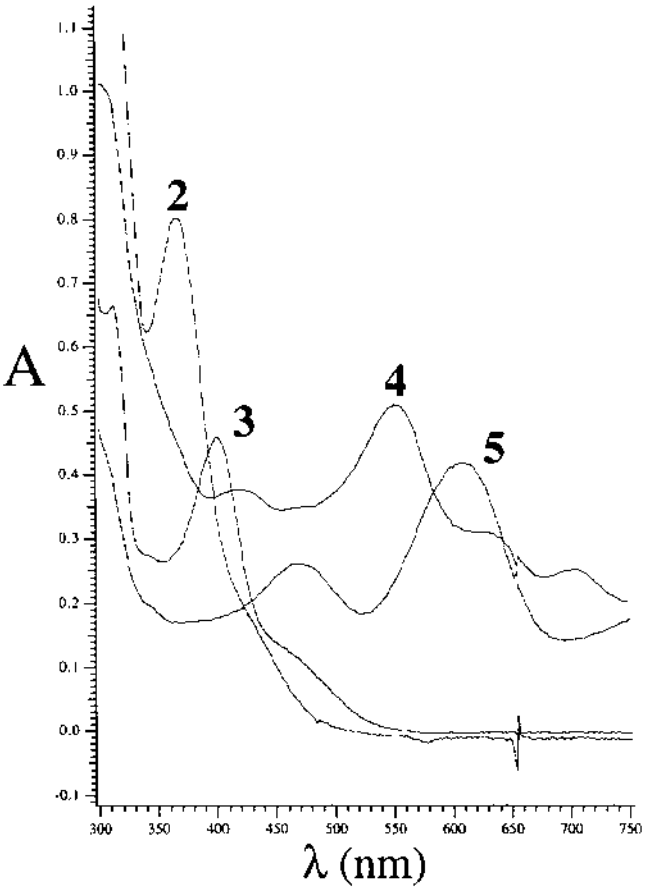

Fig. 1. UV-vis spectra in CH_3CN of **2**, **3**, **4** and **5**. Complex, Concentration (M), λ_{max} (nm), ϵ: **2** 1.48×10^{-4} 365, 5410; **3** 5.51×10^{-5} 400, 8320; **4** 1.05×10^{-4} 533, 5160; **5** 4.16×10^{-5} 471, 6270–609, 10 050.

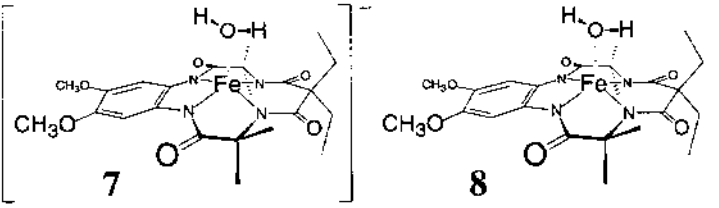

group is distorted and the average aromatic-C–N distance is short (1.374 Å) suggesting, as in **8**, [20] that the oxidation site of the molecule is more localized on this segment of the ligand than on the Fe atom.

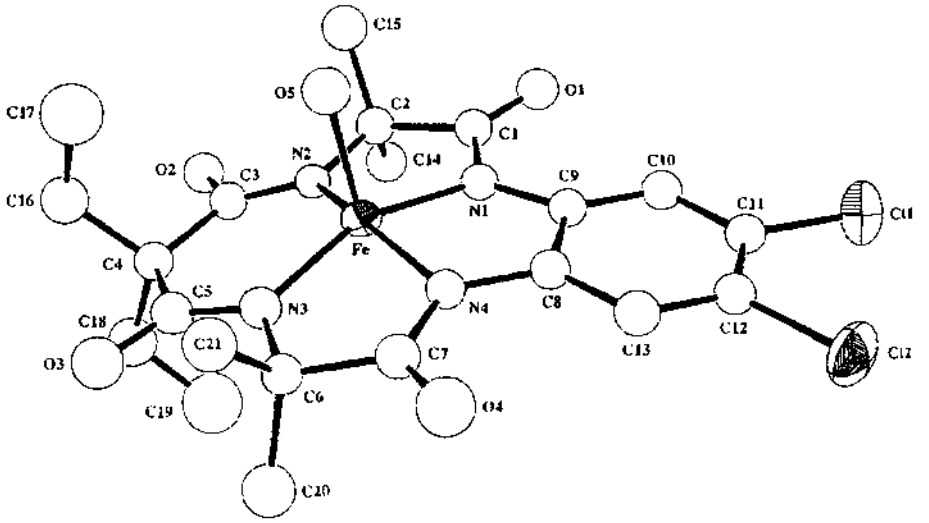

Fig. 2. X-ray crystal structure of 3. Selected bond lengths (Å): Fe–N1 1.858(8), Fe–N2 1.894(7), Fe–N3 1.867(8), Fe–N4 1.889(7), N1–C9 1.401(11), N4–C8 1.395(12), C8–C9 1.413(13), C9–C10 1.369(13), C10–C11 1.394(14), C11–C12 1.386(13), C12–C13 1.357(14), C8–C13 1.401(13), C11–Cl1 1.722(11), C12–Cl2 1.743(10).

2.3. *Mössbauer and EPR studies*

X-band EPR spectra were studied of $[Et_4N]$ [3] dissolved in various solvents. Although the essential features of the spectra were largely independent of the solvent, the best resolution was obtained in ethanol. The low temperature spectra of **3** in ethanol, displayed in Fig. 4, exhibit resonances at $g=5.8$, 5.0, 2.9 (a broad derivative feature) and $g\approx 1.8$–1.9.

Such signals are characteristic of $S=3/2$ systems for which the zero-field splittings (D, E) are large compared with the Zeeman interaction. The spectra observed here can be described by,

$$H_e = D\{S_z^2 - S(S+1)/3 + E/D(S_x^2 - S_y^2)\} + \beta S \cdot g \cdot H \quad (1)$$

For $\beta H < |D|$, the system consists of two Kramers doublets separated in energy by $\Delta = 2D\sqrt{1+3(E/D)^2}$. Each doublet yields an EPR spectrum describable by effective g-values that depend on the rhombicity parameter E/D and on $\boldsymbol{g}$. It can be seen from Fig. 4 that the intensity of the $g=5.8$ resonance increases with increasing temperature; hence, this resonance belongs to the excited state doublet, implying $D>0$. The EPR spectra also show that the resonances are significantly broader at higher applied fields. This broadening reflects g-strain which, for the present case, can be reasonably well described by assuming that the rhombicity parameter is distributed about a mean value of $E/D=0.19$ by $\sigma E/D\approx 0.06$ (for $S=3/2$ spectra this point has been discussed); the experimental data indicate the presence of a minor impurity around $g=2$ that distorts the high field feature of the $S=3/2$ system.

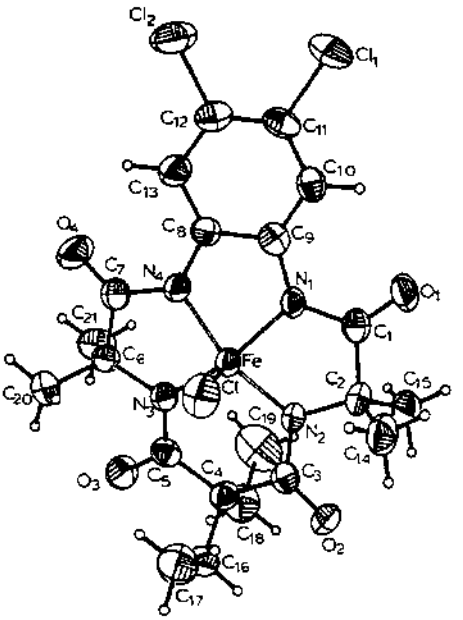

Fig. 3. X-ray crystal structure of **4**. Selected bond lengths (Å): Fe–Cl 2.203(1), Fe–N1 1.865(3), Fe–N2 1.869(3), Fe–N3 1.876(3), Fe–N4 1.864(3), N1–C9 1.376(6), N4–C8 1.372(5), C8–C9 1.425(6), C9–C10 1.396(6), C10–C11 1.373(6), C11–C12 1.393(7), C12–C13 1.375(7), C8–C13 1.396(6), C11–C11 1.730(5), C12–C12 1.728(5).

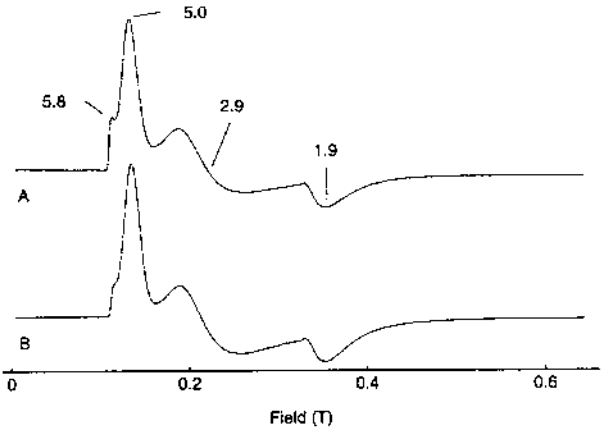

Fig. 4. Low temperature EPR spectra of complex **3** dissolved in ethanol recorded at $T=20$ K (upper trace) and $T=4$ K. Spectra were recorded at 9.46 GHz at a microwave power of 80 mW (upper trace) and 0.5 mW (lower).

The Mössbauer spectra of **3** as a solid and dissolved in ethanol are quite similar but not identical. While both samples displayed the same isomer shift, namely $\delta = 0.12\ \text{mm s}^{-1}$ at 4.2 K, the crystalline material had, at 4.2 K, a quadrupole splitting $\Delta E_Q = 4.30\ \text{mm s}^{-1}$ while the sample frozen in ethanol exhibited $\Delta E_Q = 4.00\ \text{mm s}^{-1}$. We have considered as an explanation for the difference in the Mössbauer parameters a process whereby the axial water ligand is exchanged for a molecule of solvent. However, the quadrupole splitting differences alone do not necessarily support such a process and the differences could be due to other factors such as as changes in the solvation. Thus, presently we do not have unambiguous evidence for a metathesis process when **3** is dissolved in ethanol solution.

Representative Mössbauer spectra of **3** dissolved in ethanol are shown in Fig. 5(a)–(c). In order to analyse these spectra, the Hamiltonian of Eq. (1) has to be amended by terms describing the hyperfine interactions of the electronic system with the ^{57}Fe nucleus,

$$H_{hf} = S \cdot A \cdot I + (eQV_{zz}/12)\{3I_z^2 - I(I+1) + \eta(I_x^2 - I_y^2)\} - g_n\beta_n H \cdot I \qquad (2)$$

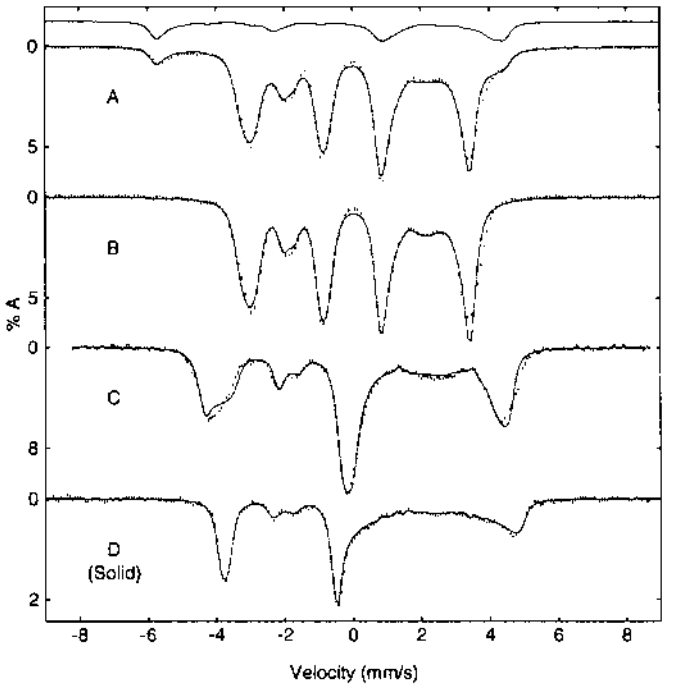

Fig. 5. Mössbauer spectra of ^{57}Fe-enriched **3** dissolved in ethanol (a)–(c) and polyerystalline **3** (d). The spectra in (a) and (b) were recorded in a parallel applied field of 0.05 T at 4.2 K (a) and 1.5 K (b). (c) Spectrum recorded at 4.2 K in an 6.0 T field applied parallel to the observed γ-radiation. The solid lines are theoretical curves generated from Eqs. (1) and (2) with the parameter set listed in Table 1. The solid line drawn above the 4.2 K low field spectrum (a) shows the contribution of the upper Kramers doublet of the $S = 3/2$ system. The spectrum of polyerystalline **3** (d) was recorded at 4.2 K in a parallel applied field of 6.0 T.

where all symbols have their conventional meanings. If the electronic spin relaxation rate is slow compared to the nuclear precession frequencies, each Kramers doublet, for $\beta H < |D|$, produces its own Mössbauer spectrum with an intensity proportional to the population of the respective doublet. This can be used to determine the zero-field splitting parameter D. The spectrum of Fig. 5(b), recorded at 1.5 K in a parallel field of 0.05 T, results from the electronic ground doublet. At 4.2 K, the upper Kramers doublet is partially populated, contributing a spectrum whose shape is outlined by the solid line drawn above the spectrum of Fig. 5(a). By adjusting the relative intensities of the two spectral components, we obtained $D = +2.4 \pm 0.2\ \mathrm{cm}^{-1}$. From a group fit to the spectra shown in Fig. 5(a)–(b), we obtained the rhombicity parameter, $E/D = 0.21$.[1] The solid lines shown in Fig. 5(a)–(c) are simulated spectra obtained by solving $H = H_e + H_{hf}$. The parameters thus obtained are listed in Table 1.

The parameter set obtained for **3** in ethanol shows that the magnetic hyperfine tensor and the electric field gradient tensor are axially symmetric and collinear. The symmetry axis of both tensors is along the y-direction of the zero-field splitting tensor, i.e. along the direction for which one would observe the $g_y = 5.0$ resonance in an EPR experiment with a single crystal of **3**. Note that **3** has a very large quadrupole splitting, $\Delta E_Q = 4.0\ \mathrm{mm\ s}^{-1}$; this splitting was found to be independent of temperature up to 150 K. While a large ΔE_Q is typical for intermediate-spin Fe^{III} complexes, a theory that explains these unusually large values has not yet been published. The magnetic hyperfine tensor is quite anisotropic, a reflection of substantial spin–dipolar contribution. By averaging the components of A, the spin–dipolar contribution cancels and we may obtain a good estimate for the isotropic contact term, $A_c = (A_x + A_y + A_z)/3 = -13.1$ MHz. Finally, the isomer shift of **3** is $\delta = 0.12\ \mathrm{mm\ s}^{-1}$ at 4.2 K. This value is at the very low end of $S = 3/2$ complexes published values for δ range from 0.14 to 0.35 $\mathrm{mm\ s}^{-1}$ [20,21,29–31].

Spectra of polycrystalline **3** recorded in zero-field exhibit a sharp quadrupole doublet with $\Delta E_Q = 4.30\ \mathrm{mm\ s}^{-1}$ and $\delta = 0.12\ \mathrm{mm\ s}^{-1}$ at 4.2 K. ΔE_Q is nearly independent of temperature. We have studied the polycrystalline compound at 4.2 and 1.5 K over a wide range of applied magnetic fields. Fig. 5(d) shows a 6.0 T spectrum recorded at 4.2 K; the solid line is a theoretical curve obtained with the parameters listed in Table 1. The quoted parameters fit the 6.0 T spectra quite well. However, as the applied field was lowered, the magnetic splittings were observed to decrease more rapidly than predicted by Eqs. (1) and (2) for *any* values of the zero-field splitting parameters. By assuming weak intermolecular antiferromagnetic exchange, $J \approx 0.5\ \mathrm{cm}^{-1}$ for $H = JS_1 \cdot S_2$, between pairs of molecules, we have been able to model

[1] This value is more reliable than the value that can extracted from EPR. The magnetic hyperfine splittings observed in the Mössbauer spectra depend on the expectation values of the electronic spin. In weak applied fields, these values depend critically on E/D, but are independent of the g-tensor of Eq. (1). In contrast, the EPR resonances depend sensitively on both E/D and g. A least-squares fit to the entire set of Mössbauer spectra suggests $E/D = 0.21 \pm 0.02$. We have finally chosen $E/D = 0.19$ because this value allows one to fit the EPR resonances to Eq. (1) without using excessively large values for g. By choosing $g_x = 2.05$, $g_y = 2.00$ and $g_z = 2.01$ in Eq. (1), we obtain $g_x = 2.9$, $g_y = 5.0$ and $g_z = 1.8$ for the ground doublet and $g_x = 1.2$, $g_y = 1.0$ and $g_z = 5.8$ for the excited state. These values are in good agreement with the data.

Table 1
Parameters derived from Mössbauer data for compounds **3** and **5**

	D (cm^{-1})	E/D	g_x[a]	g_y	g_z	A_x (MHz)	A_y (MHz)	A_z (MHz)	ΔE_Q[b] (mm s^{-1})	η	δ (mm s^{-1})
3 (solid)	2.5 (15)	c	2	2	2	−22(1)	+11 (1)	−28 (7)	4.25 (5)	+3	0.12 (2)
3 (EtOH)	2.4 (2)	0.21 (2)	2.05	2.00	2.01	−23(2)	+9.2	26(2)	−4.0 (1)	2.7	0.12(4)
5 (solid)	22 (2)	0	2.24	2.24	1.99	−30(1)	−30(1)	−4 (3)	4.35 (2)	0	−.18(2)

[a]The Mössbauer spectra are quite insensitive to the g-values. For polycrystalline **3** we have set $g=2.0$. For the g-values of the solution sample of **3**, see Ref. [20]. The g-values for **5** were determined from D and E/D with the help of the ligand field model of Oosterhuis and Lang (see text).
[b]The A-tensors and the quadrupole tensors are quoted in the frame of the zero-field splitting tensor. For the ferric complexes, the field gradient tensor is nearly axial with the symmetry axis pointing along the x-axis of the zero field splitting tensor. Quoted in the principal axis frame of the field gradient tensor, the values $\Delta E_Q=-4.25$ mm s^{-1} and $\eta=+3.0$ translate into $\Delta E_Q=+4.25$ mm s^{-1} and $\eta=0$.
[c]The choice of the best E/D value depends on the choice of D. For the simulation shown in Fig. 5(d), the exact choice of D and E/D is not critical; we have used $D=2.4$ cm^{-1} and $E/D=0.21$.

the field dependence over the entire range of applied fields. For $J<1\ cm^{-1}$, the 6.0 T spectrum of Fig. 5(d) is essentially independent of J [32,33].[2] The parameters quoted for polycrystalline **3** are very similar to those recently reported by us [20] for the polycrystalline Fe^{III}–H_2O complex with methoxy substituents, **7**.

Fig. 6 shows a series of Mössbauer spectra of the Fe–cyano complex, **5**, recorded between 4.2 and 150 K in zero field [Fig. 6(a)] and in parallel applied fields of 8.0 T. The 4.2 K zero field spectrum, shown in Fig. 6(a), consists of a sharp doublet with a very large quadrupole splitting, $\Delta E_Q=4.35\ mm\ s^{-1}$, and isomer shift,

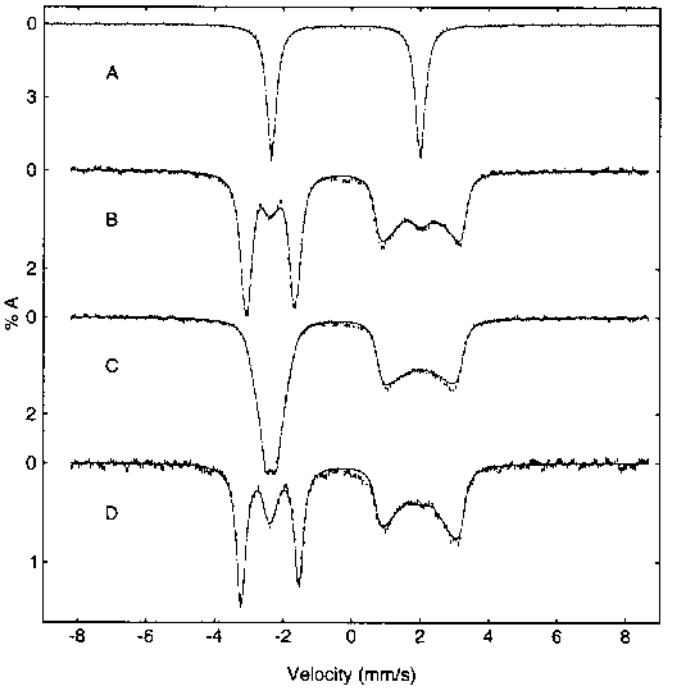

Fig. 6. Mössbauer spectra of a polycrystalline sample of the Fe^{IV}-cyano complex, **5**. The spectra were recorded at 4.2 K in zero field (upper spectrum) and in parallel applied fields of 8.0 T at temperatures indicated. The solid lines are theoretical curves generated from Eqs. (1) and (2) for $S=1$ using the parameters listed in Table 1.

[2]We have recently observed intermolecular exchange interactions, up to $J=20\ cm^{-1}$ [32], for a variety of tetraamide complexes. Moreover, the low temperature EPR spectra of polycrystalline samples of the ferric parent compound of **3a** display complex patterns that suggest a perturbation of the $S=3/2$ manifold by weak exchange. The X-ray structure of **3** shows two cofacial molecules in the unit cell, well separated by couterions, with an Fe–Fe distance of 12.9 Å. This distance seems too large to account for a J-value of $0.5\ cm^{-1}$, if J reflects indeed a dimer–dimer interaction. A somewhat similar situation has been reported by Gupta et al. [33]for the tetraphenylporphyrin complex $Fe(TPP)(SbF_6)\cdot C_6H_5F$ (nearest Fe–Fe distance = 10.3 Å). In order to fit the Mössbauer and susceptibilty data for this complex, a J-value of $1.39\ cm^{-1}$ was required; the authors have suggested that this value may reflect the interaction of a porphyrin molecule with n (=10) neighbours, in which case $J=nj$ where j measures the interaction between pairs.

$\delta = -0.18$ mm s^{-1}. These parameters, especially the negative value of δ, are characteristic of $S=1$ Fe^{IV} complexes. The applied field spectra exhibit paramagnetic hyperfine structure, confirming that $S \neq 0$. Moreover, these spectra indicate that the electronic spin relaxation rate is fast, implying that the magnetic hyperfine field at the ^{57}Fe nucleus, $H_{int}(i) = - < S_i >_{th} A_i/g_n\beta_n$ $(i = x, y, z)$, is proportional to the thermally averaged electronic spin, $\langle S \rangle_{th}$. ΔE_Q was found to be independent of temperature, showing that no excited orbital states are appreciably populated at the temperatures of measurement. Thus, $\langle S \rangle_{th}$ is determined by averaging over the sublevels of the $S=1$ multiplet. At 150 K, $\langle S_i \rangle_{th} \approx 0.05$ (at 8.0 T) is nearly independent of the zero-field splitting of the $S=1$ multiplet. Analysis of the 150 K spectrum of Fig. 6(d) then provides the sign (ΔE_Q), η, and good estimates for the components of the A-tensor. With this information, the low temperature Mössbauer spectra yield reliable values for D and E. Our analysis shows that the tensor quantities of Eqs. (1) and (2) are axial and collinear, suggesting that the Fe–C–N axis is perpendicular to the plane made by the four N-donors of the tetraamide ligand. The solid lines in Fig. 6 are theoretical curves computed with the parameters listed in Table 1.[3]

Using crystal field theory for the t_{2g}^4 configuration, Oosterhuis and Lang published in 1973 useful perturbation expressions for the zero-field splitting tensor, the g-tensor and the A-tensor [34]. In the limit of axial symmetry, the zero-field splitting parameter D and the g-values are given by $D = \xi 2/4\Delta$, $g_{x,y} = 2.0 + \xi/\Delta + \xi^2/2\Delta^2$, and $g_z = 2.0 - \xi^2/4\Delta^2$, where $g = 400$ cm^{-1} is the one-electron spin–orbit coupling constant and Δ is a tetragonal splitting that separates the one-electron d_{xy} ground singlet from the degenerate excited orbital (d_{xz}, d_{yz}) pair (see Fig. 1 [34]). For the quoted value of ξ and $D = 22$ cm^{-1}, the two (degenerate) excited orbital states of the system would be at 1800 cm^{-1}. These levels are too high to be populated at 150 K, in accord with our observation that ΔE_Q is independent of temperature. Since the Mössbauer spectra are not very sensitive to the g-values, we have used the g-values predicted by the deduced ξ/Δ ratio for the final fits of the spectra of **5**, namely, $g_x = g_y = 2.24$ and $g_z = 1.99$.

3. The Fe(III)–TBHP–nitrile system

3.1. Analysis of the inorganic components

The **3**–nitrile–TBHP system yielded two end products derived directly from **3**. When $[Et_4N]_2$**2** or $[Et_4N]$**3** were dissolved in an aliphatic nitrile solvent containing an α–CH or α–CD bond (CD_3CN, CH_3CN, CH_3CH_2CN, $(CH_3)_2CHCN$), addition of TBHP caused a deep blue color to form in the solution. The blue color was not found with $(CH_3)_3CCN$ as the solvent, a nitrile without α–CH bonds. If base was

[3] A large number of Mössbauer spectra were obtained characterizing the "blue species" prepared in acetonitrile solution. A complex was observed (75–90% of total Fe) with $\Delta E_Q = 4.4$ mm s^{-1} and $\delta = -0.15$ mm s^{-1}. The applied field spectra of this species were quite similar to those of Fig. 7, suggesting that the complex was the solution form of **5**.

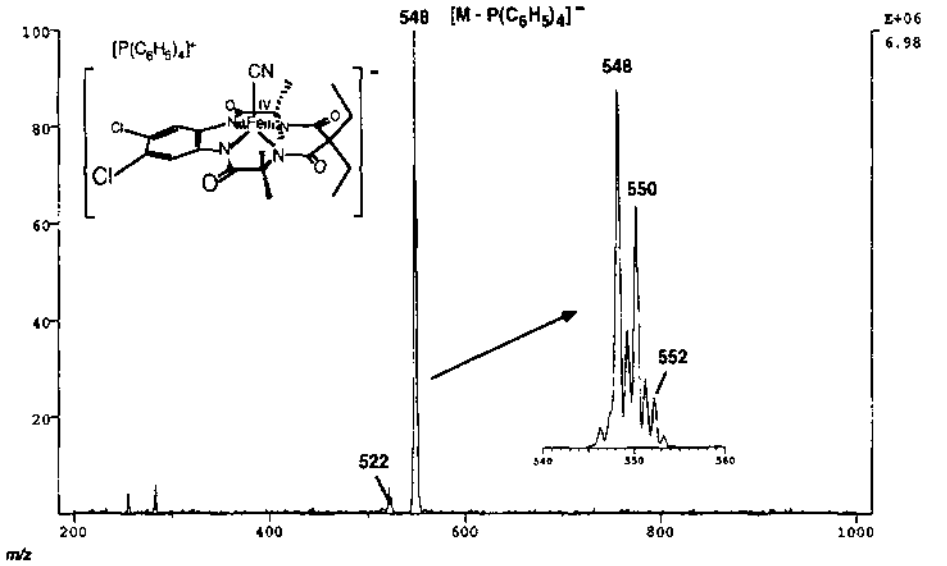

Fig. 7. ESI mass spectrum of the anion **5**. Insert: expansion of molecular anion region, the isotope pattern is appropriate for the formulation [M-CN]$^-$.

present at the beginning of the reaction, or if it was added following formation of the blue color, the blue color persisted.[4] Removal of the solvent in vacuo, and addition of water yielded a blue homogeneous solution. Addition of [PPh_4]Cl yielded a blue precipitate, a mixture comprised predominantly of the Fe^{IV} axial cyanide complex [PPh_4]**5**, and a minor amount of the ligand degradation product **6**, which is an iron free species. Formation of the blue color was the visible manifestation of a complicated reaction sequence involving catalytic oxidation of the nitrile solvent. For the remainder of this paper, we will focus on identification of the two components that come from the iron starting material, **5** and **6** and we will defer extensive data we have obtained on the organic product analysis to a later publication.

3.2. Identification of an Fe(IV) CN complex product

A formulation for the major blue product formed in the **3**–nitrile–TBHP system was obtained from ESI-MS data (Fig. 7). Both the isotope pattern of the predominant ion cluster and the observed mass–charge ratio could be realistically explained only by assignment of the principal ion to a singly charged monomeric axial Fe^{IV}–cyano complex; Fe^{IV}–cyano complexes have been previously reported [28,35]. Once a formulation of the blue product had been obtained, it then became possible

[4] In the absence of base, the blue color slowly turned yellow-brown. This final color change has not been pursued for this report beyond the determination by IR spectroscopy that it does not result from a quantitative conversion of **5** to the 1723 cm^{-1} band-producing product. The role of the base in preserving the blue material is not accurately defined at this point.

to devise an alternative synthesis of $[PPh_4]$**5** to test the assignment. Treatment of the structurally characterized, $S=1$, chloride complex, $[Et_4N]$**4** (Fig. 3), with cyanide ion in water, cleanly yielded a deep blue species which could be precipitated quantitatively on addition of $[PPh_4]Cl$. The UV–vis spectra of $[PPh_4]$**5** obtained from either route showed the same bands and relative intensities; however, the ϵ values were slightly larger for the material derived from the **4**–H_2O–CN^- synthesis.

Further substantiation of an Fe^{IV}–CN formulation for **5** was obtained by IR and ESI-MS analysis of isotopically labeled samples. When $[PPh_4]$**5** was prepared from **3**–nitrile–TBHP in CH_3CN or in CH_3CN–$CH_3{}^{13}CN$ (1:1), the IR spectra of the two solids were identical except in the $\nu(C\equiv N)$ region (2050-2150 cm^{-1}) (Fig. 8). Both spectra contained a weak band for $\nu(^{12}C\equiv N)$ at 2129 cm^{-1} while the sample prepared in CH_3CN–$CH_3{}^{13}CN$ contained an additional band at 2082 cm^{-1} for $\nu(^{13}C\equiv N)$ of equal intensity to the $\nu(^{12}C\equiv N)$ band. Preparation of $[PPh_4]$**5** from **4**–H_2O–NaCN yielded an identical IR spectrum in the $\nu(C\equiv N)$ region as compared with that prepared from **3**–CH_3CN–TBHP (Fig. 8) while that prepared from **4**–H_2O–$Na^{13}CN$ showed only the expected $\nu(^{13}C\equiv N)$ band at 2082 cm^{-1} (Fig. 8). The IR spectrum of $[PPh_4]$**5** prepared from **4**–H_2O–$KC^{15}N$ is also shown in Fig. 8. The bands for the three isotopomers shift according to Hooke's law for a CN group. Moreover, ESI mass spectra of $[PPh_4]$**5** prepared in the mixed solvent and of $[PPh_4]$**5** prepared with $^{13}CN^-$ show the expected additional peak at m/z 549 for the ^{13}C–labeled axial cyanide complex.

3.3. Identification of an organic hydantoin product

Mössbauer spectroscopy of $[PPh_4]$**5** showed the same principal species regardless of synthetic route, (Fig. 6). However, samples of $[PPh_4]$**5** prepared from **3**–nitrile–TBHP revealed the presence of an additional $S=5/2$ Fe^{III} species (ca. 10%

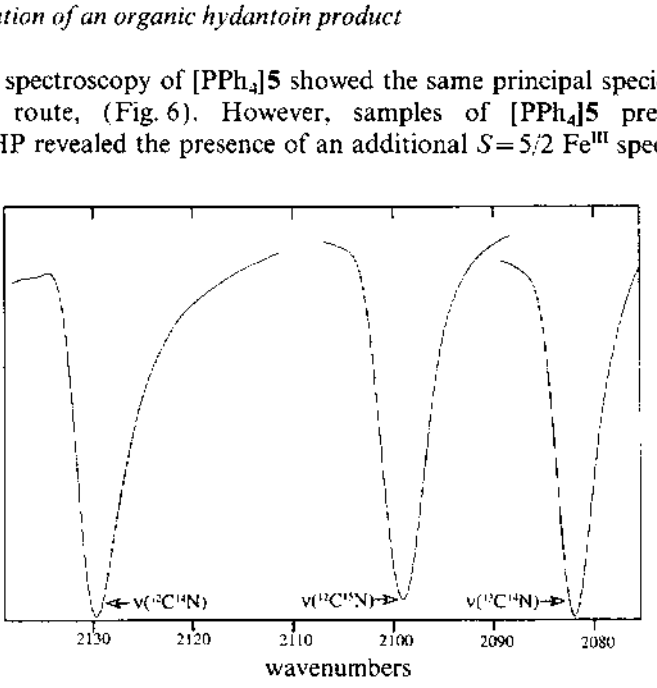

Fig. 8. IR spectra showing the ν(CN) region for $[PPh_4]$**5** with $^{12}C^{14}N^-$, $^{12}C^{15}N^-$, and $^{13}C^{14}N^-$ ligands.

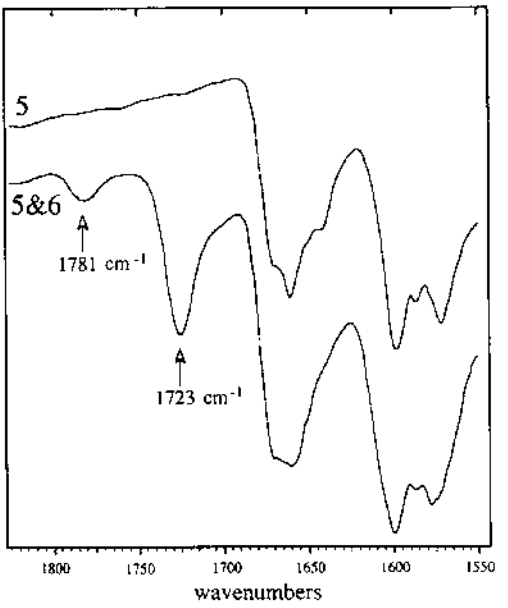

Fig. 9. IR spectra [nujol mull] in amide region, $[PPh_4]$**5** (top) and Mixture of $[PPh_4]$**5** and **6** (bottom).

of total iron). Iron(III) complexes of tetraamido-*N*-donor ligands have $S=3/2$, therefore, the $S=5/2$ Fe^{III} species is likely to arise from a free Fe^{III} species. This implicated the presence of a ligand decomposition pathway in the **3**–nitrile–TBHP system. Samples of $[PPh_4]$**5** exhibited the same molecular anion by ESI-MS (Fig. 7) independent of route. However, the IR spectra of the two materials were different in one significant respect; the spectrum of $[PPh_4]$**5** prepared from **3**–nitrile–TBHP exhibited a strong band at 1723 cm^{-1}, while this band was absent in the IR spectrum of $[PPh_4]$**5** prepared from **4**–cyanide (Fig. 9). These results suggested that $[PPh_4]$**5** prepared from **3**–nitrile–TBHP contained at least one additional species, **6**, probably derived through a ligand degradation process and with a characteristic IR band at 1723 cm^{-1}.

Attempts to separate the components present in $[PPh_4]$**5** prepared from the **3**–nitrile–TBHP system by chromatography on silica gel were unsuccessful. However, separation of the components present in the related $[Et_4N]$**5** prepared from the **3**–nitrile–TBHP system yielded two principal components: a colorless diamagnetic compound present in small quantities (< 10% of total mass), **6**, and a blue compound that was shown to be $[Et_4N]$**5**.[5] Preliminary ^1H and ^{13}C NMR spectra of **6** were similar to the parent tetraamido macrocyclic ligand, but some notable differences were also observed. In the ^1H NMR spectrum of **6**, three exchangeable amide resonances and a quartet at 6.25 ppm with coupling to a doublet at 1.70 ppm ($J=$

[5]Several other bands are found on the TLC plates. A yellow-brown origin material and a second colorless species that is present in ca. 10% of compound **6**.

7 Hz) suggested the presence of an olefinic CH coupled to a geminal CH_3 group along with a loss of the observed symmetry of the parent tetraamide. FAB-MS data indicated that the monoisotopic molecular mass of **6** was 468 Da, as evidenced by the moderately intense ions at *m/z* 469, 471 and 472, with the appropriate relative intensities for two chlorine atoms. Combination of FAB-MS, NMR and elemental analysis data for **6** were consistent with the two formulations shown in Fig. 10.

In order to convincingly distinguish between the two formulations of Fig. 10, a combination of mass spectrometric techniques were utilized in conjunction with deuterium labeling of **6**. High resolution accurate mass analysis of the experimentally observed fragment ions allowed an unambiguous assignment of **6** to the hydantoin-containing structure. Full details of the analysis are presented in the experimental section.

In the IR spectrum of pure **6**, the 1723 cm^{-1} band was found to be much stronger than bands arising from the stretching vibrations of the other carbonyl-containing fragments (Fig. 11). This explains why the band was clearly visible in the IR spectrum of $[PPh_4]$**5** samples in which **6** was present as a minor component. The IR spectrum of the parent dimethylhydantoin heterocycle is shown in the inset to Fig. 11; its features in the 1600–1800 cm^{-1} region suggested that the relatively weak band at 1781 cm^{-1} also arose from the dimethylhydantoin group of **6**. We now turn to evidence from the product distribution that suggests how **6** might be formed.

3.4. Proposed mechanism of ligand degradation (how is the hydantoin formed?)

In IR spectra of $[PPh_4]$**5** prepared from different nitriles, the ratios of the intensities of the 1723 cm^{-1} band arising from **6** to the intensities of the amide bands arising from **5** varied with the choice of solvent–substrate. After the number of α-CH substituents was accounted for, the relative intensity of the 1723 cm^{-1} band was found to decrease through the series CD_3CN, CH_3CN, CH_3CH_2CN, $(CH_3)_2CHCN$, i.e. as the solvent became more easily oxidized by H-atom abstraction.

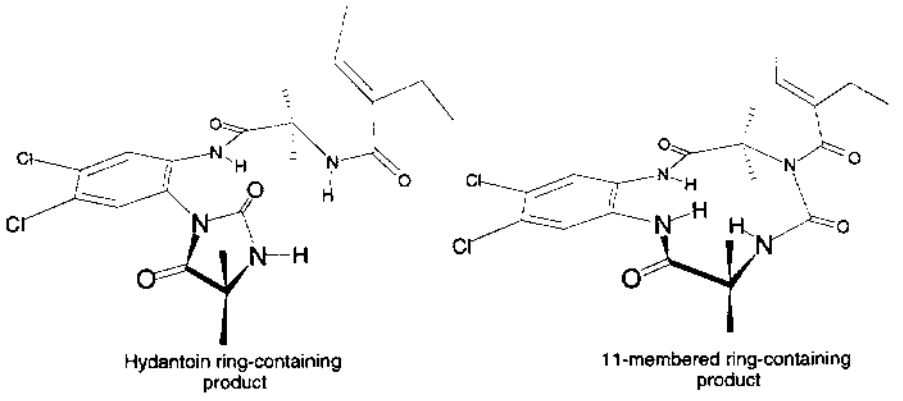

Fig. 10. Possible formulations for 1723/1781 cm^{-1}-producing impurity based on ^1H and ^{13}C NMR and FAB-MS data.

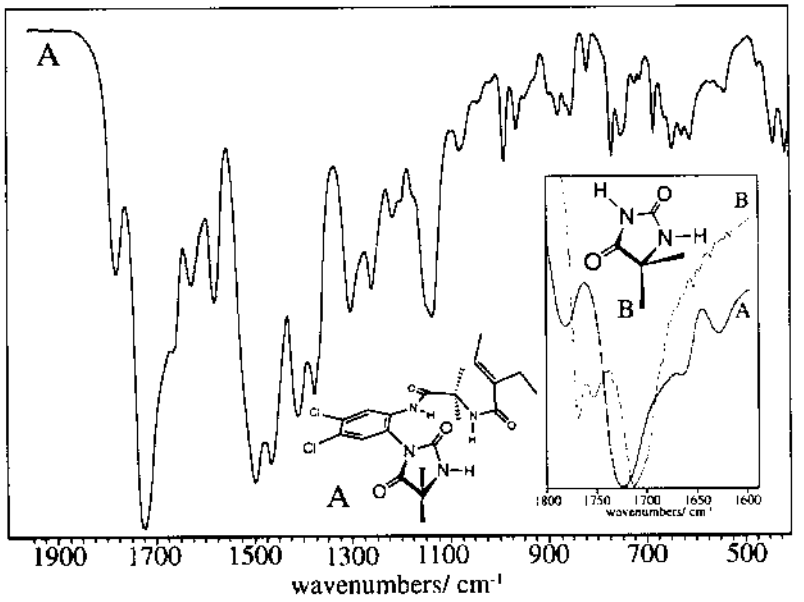

Fig. 11. The IR spectrum of solid **6** showing the strong 1723 cm^{-1} band. Insert: comparison of the 1600–1800 cm^{-1} region of **6** [**A**] and the parent dimethylhydantoin heterocycle [**B**].

This is consistent with the solvent-substrate and the ligand ethyl group competing for reaction with an H-atom abstracting entity in the reaction system with the latter attack leading to the ligand degradation product **6**. Such an H-atom abstracting entity could be either an Fe–oxo moiety two equivalents oxidized above the Fe^{III} state [36,37][6] or a *t*-butyloxyl radical. We do not yet have sufficient evidence to directly identify the oxidizing entity, although we are attempting to identify the postulated Fe–oxo species by low temperature trapping experiments. The fact that the same tetraamido-*N* macrocycle effectively stabilizes a Mn^{V}–oxo complex, which is also produced by TBHP oxidation of a lower valent complex, [23–25] provides an additional suggestion that an Fe–oxo complex be the main oxidizing entity. The suggestion of Fe–oxo oxidizing intermediates in hydrocarbon oxidations is a subject of controversy in the literature [13–18].

A proposed mechanism presenting an oxidized iron complex to account for the observed C–H bond activation of the ligand is shown in Scheme 2. In this mechanism, the putative abstracting entity is an Fe–oxo intermediate, **A**. It is suggested that the Fe–oxo group of **A** abstracts a methylene H-atom from an ethyl ligand substituent to produce an Fe^{IV}–hydroxo complex that also has a ligand carbon-centred radical,

[6]Other mechanisms could account for the ligand oxidation. In two recent interesting articles, proposals were made that O–O bond scission in metal peroxy species is accompanied by a C–H bond cleavage in the formation of the transition state, i.e. a free oxo species is not formed. However, the low valent metal centre of the peroxy species that is cleaved in each case (Co^{I}–d^{8} and Cu^{II}–d^{9}) does not have available empty orbitals at the metal for formation of metal-oxo π-bonds.

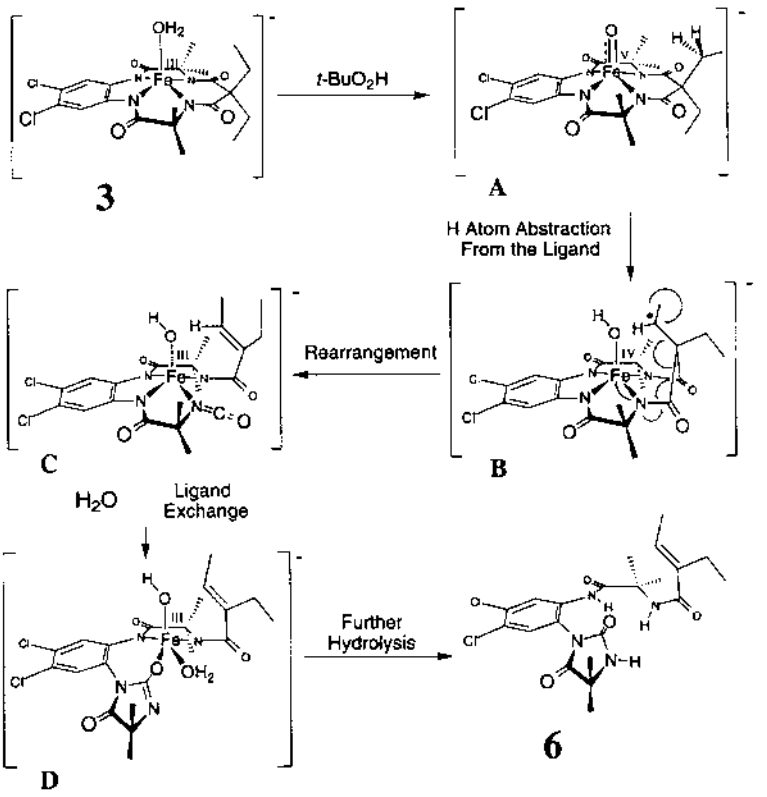

Scheme 2. Proposed ligand oxidative degradation scheme. In the scheme, we have drawn an Fe^{V}–oxo intermediate, A. With this, we do not wish to imply any specific allocation of oxidizing equivalents to the metal or the ligand. Alternative formulations include an Fe^{IV}–oxo/ligand radical cation. In addition, the abstracting entity could be a free radical.

B. Molecular models suggest that, in a boat conformation of the six-membered chelate ring, the methylene H-atoms can be oriented to be within easy reach of the proposed iron–oxo O-atom. Since O_2 is present during the reaction sequence and is likely to couple with the radical species present in **B** at close to diffusion controlled rates, we propose further that **B** must rapidly decompose. This follows because **5** is the only ligand degradation compound produced in significant quantity. If **B** had a significant lifetime, one might expect to find additional blue complexes related to **5**, but containing an oxygenated methylene group, e.g. an alcohol or a ketone substituted ligand (all hydroperoxides are decomposed in the reaction system). The proposal of a rapid decomposition is chemically acceptable if the radical-bearing metallocycle is ring-strained, an entirely plausible assumption. Therefore, we propose that the six-membered ring with the exocyclic radical rapidly opens to produce the Fe^{III}-*N*-isocyanate ligand, **C**. The isocyanate ligand of **C** is then proposed to condense with the adjacent amido-*N* ligand in the ring-opened chelate to afford the

Fe^{III}-*O*-hydantoin ligand complex, **D**. Finally, it is suggested that **6** is liberated from the metal by hydrolysis involving the ample water supply present in the system. For a free radical abstraction of the H-atom leading to **B**, only the first step would be considered to be different.

4. Conclusion

The current report presents one component of a complex reactivity sequence that arises in the **3**–nitrile–TBHP system, namely, that portion of the sequence that can be elucidated by an analysis of the inorganic and ligand-associated components of the reaction manifold. The products derived from **3** in the **3**–nitrile–TBHP system have been identified as **5** and **6**, and a mechanism has been postulated for the formation of **6**. Additional questions concerning the mechanism of oxidation of the nitrile solvent–substrate and the manner in which the iron compound captures a cyano group from the solvent have also been the subject of an extensive investigation; these studies will be deferred to a subsequent paper.

The work described herein has several aspects. First, novel oxidized iron complexes including the Fe^{IV}–CN complex, **5**, have been attained and characterized and it is interesting that exchange of the Cl^- ligand of **4** for the more strongly σ-donating CN^- ligand produce a shift in the oxidation site from the ligand to the metal. Second, while the system consumes all the hydroperoxide and carries out a significant amount of nitrile C–H oxidation, the macrocyclic ligand system remains substantially intact. Moreover, the high selectivity found in the ligand degradation process suggests that the design of the current macrocylic tetraamide is nearly appropriate for supporting a long-lived metalloredox-active catalytic system for C–H bond oxidations, an indication that has been supported by further studies. Thus, we have found (S.W. Gordon-Wylie, C.P. Horwitz, L.D. Vuocolo and T.J. Collins, unpublished results) that the simple exchange of ethyl groups on the six-membered ring of **3** with methyl groups produces a catalyst system in which hydantoin degradation is not observed under the conditions of the oxidation catalyses described herein; the analogue of **5** is the sole inorganic product. When this new catalyst system is treated with TBHP in a robust solvent such as CH_2Cl_2 a hydantoin degradation product is obtained with a signature IR band at 1721 cm^{-1}. The longer lifetime of the dimethyl- versus diethyl-substituted six-membered ring can be attributed to the increased C–H bond strength of the abstracted H-atom. Based upon the C–H bond strengths of propane, $D(CH_3C\underline{H}_2CH_3) = 95 \pm 1$ kcal mol^{-1}, $D(CH_3CH_2C\underline{H}_3) = 98 \pm 1$ kcal mol^{-1}, [38] one would expect the ligand methyl group to have a bond strength ca. 3 kcal mol^{-1} greater than the ligand ethyl. The ethyl for methyl substitution produces a greatly enhanced catalyst lifetime when the new catalyst is used to activate hydrogen peroxide in water at basic pH and at room temperature for a variety of oxidations. Studies of dye oxidations with the new catalyst system are currently being disclosed [39].

Finally, it is interesting to reflect on the relative reactivity of the well-characterized Cr^V–oxo and Mn^V–oxo analogues of the iron species that we have suggested might

be responsible for the observed ligand degradation. In contrast with unreactive families of d^1 Cr^V–oxo [40] and d^2 Mn^V–oxo [23,24] complexes that we have produced with macrocyclic tetraamides, the proposed Fe–oxo analogue, which would be two equivalents oxidized above the Fe^{III} state, appears to be a very reactive H-atom abstractor. Assuming such a species is indeed the actual oxidant in the **3**–nitrile–TBHP system, we suggest that the additional electron in the iron system compared with the manganyl plays a significant role in the increased reactivity. While the one d-electron of the $S=1/2$ Cr^V–oxo complexes and the two d-electrons of the $S=0$ Mn^V–oxo complexes occupy the nonbonding d-orbital lying approximately in the plane of the macrocyclic ligand, the additional electron of the Fe–oxo complex would be housed in an orbital that is π^* in character with respect to the Fe–O bond; this should place significant radical character directly on the oxo ligand, predisposing the oxo complex towards H-atom abstraction. We anticipate such Fe–oxo systems would show variable reactivity as changes in macrocyclic substituents modify the donor capacity of the ligand and, by a perturbation, the energy and composition of the key radical orbital.

5. Experimental procedure

5.1. Materials and reagents

Unless otherwise indicated, solvents and reagents were Fisher reagent grade and materials were used as received. Microanalyses were performed by Midwest Microlabs, Indianapolis, IN.

5.2. Electrochemical measurements

Cyclic voltammetry was performed under N_2 in a three compartment cell using a glassy carbon disk working electrode ($A \sim 0.0078$ cm^2 or 0.071 cm^2), a Pt wire counter electrode, and an NaCl saturated calomel electrode (SSCE) as reference. CH_2Cl_2 (Aldrich Sureseal) or CH_3CN (dried over CaH_2) was employed as solvent with a supporting electrolyte of $[Bu_4N][ClO_4]$ (0.1 M, Fluka, vacuum dried 24 h, 25 °C) or $[Bu_4N][PF_6]$ (0.1 M, Fluka puriss). A Princeton Applied Research Model 273 Potentiostat–Galvanostat controlled with a Compudyne 486DX computer was used and current–voltage curves were recorded on a Graphtec Model WX1200 X-Y recorder. Alternatively, a Princeton Applied Research Model 173/179 potentiostat–digital coulometer equipped with positive feedback IR compensation and a Model 175 universal programmer was used and current–voltage curves were recorded on a Houston Instruments Model 2000 X-Y recorder. At the conclusion of some experiments, ferrocene (Fc) was added as an internal potential standard and the current–voltage curve was rerecorded. Formal potentials were calculated as the average of anodic and cathodic peak potentials and are reported versus NHE. Peak-to-peak separation of the Fc^+/Fc couple was similar to that of the iron compound couples

in all cases. Plots of peak current versus the square root of scan speed over the range 20–500 mV s^{-1} were found to be linear for all couples.

5.3. Mass spectrometry

Electrospray ionization mass spectra were acquired on a Finnigan-MAT SSQ700 (San Jose, CA) mass spectrometer fitted with an Analytica of Branford electrospray interface. Electrospray voltages of 2400–3400 V were utilized. Samples were dissolved in either acetonitrile or dichloromethane at concentrations of approximately 10 pmol μl^{-1} and were introduced into the ESI interface by direct infusion at a flow rate of 1 $\mu l\ min^{-1}$. Spectral averaging for 1–2 min was employed prior to data acquisition. Positive ion electron impact ionization (70 eV) MS experiments were performed on a Finnigan-MAT 4615 quadrupole mass spectrometer in conjunction with an INCOS data system. The ion source temperature was 150 °C and the manifold chamber temperature was 100 °C. Sample introduction was by means of a gas chromatograph or a direct insertion probe. Positive ion fast atom bombardment mass spectra were acquired on a Finnigan-MAT 212 magnetic sector instrument in combination with an INCOS data system. The accelerating voltage was 3 kV and the ion source temperature was approximately 70 °C. An IonTech saddle field fast atom gun was employed with xenon at 8 keV. Thioglycerol was utilized as the FAB matrix. Positive ion electron impact ionization (70 eV) MS–MS experiments were performed on a Finnigan-MAT TSQ700 tandem quadrupole mass spectrometer. Sample introduction was by means of a direct insertion probe. The ion source was maintained at 150 °C and the manifold chamber was held at 70 °C. Collision-induced dissociation (CID) was achieved by introducing argon into the centre rf-only collision octapole until the pressure in the manifold reached $0.9–2.5 \times 10^{-6}$ Torr. The nominal ion kinetic energy for CID product ion was <35 eV (laboratory reference). High resolution data were obtained on a JEOL JMS AX-505H double focusing mass spectrometer in the EB configuration using a resolution of 7500. Sample introduction was by means of a gas chromatograph or direct insertion probe. During mass spectral acquisition perfluorokerosene was introduced into the ion source by means of a heated inlet. Exact mass assignments were obtained by computer-assisted interpolation from the masses of perfluorokerosene.

5.4. Spectroscopic methods

300 MHz ^{1}H NMR spectra and 75 MHz ^{13}C NMR spectra were obtained on an IBM AF300 instrument using an Oxford superconducting magnet system; data acquisition was controlled by Bruker software. Infrared spectra were obtained on a Mattson Galaxy Series 5000 FTIR spectrometer controlled by a Macintosh II computer. UV–vis spectra were obtained on a Hewlett Packard 8452A spectrophotometer driven by a Zenith Z-425/SX computer. Conventional X-Band EPR spectra were recorded on a Bruker ER300 spectrometer equipped with an Oxford ESR-900 helium flow cryostat. Mössbauer spectra were obtained on constant acceleration instruments and isomeric shifts are reported relative to an iron metal standard at

298 K. In order to avoid orientation of polycrystalline samples by the applied magnetic field, the samples were suspended in frozen nujol.

5.5. Syntheses

5.5.1. Synthesis of an Fe(III) Cl and Fe(III)(H_2O) complex

The parent macrocyclic tetraamide [41] (525 mg, 1.1 mmol) was dissolved in tetrahydrofuran (40 ml, Aldrich) under N_2. *tert*-Butyllithium under N_2 (2.6 ml, 4.4 mmol, 1.7 M in 2,4-dimethylpentane, Aldrich) was added to the solution under N_2 at −108 °C. Ferrous chloride (anhydrous, 155 mg, 1.2 mmol, Alfa) was added to the mixture under N_2. The solution was allowed to warm to room temperature and was stirred (16 h), yielding an olive-green precipitate. Air was admitted through a drying tube (2 h), and the orange solid was collected and washed with CH_2Cl_2 (2 × 10 ml). The resulting orange powder was dried under reduced pressure. Yield: 595 mg (~93%). Because of variable solvation and limited solubility, the lithium salt was converted to the tetraethylammonium salt for further use. The lithium salt (595 mg) in CH_3OH (50 ml) was loaded on an ion exchange column (Dowex® 50X2-100, 25 g, 2 cm × 12.5 cm) that had been presaturated with $[Et_4N]^+$ cations, and the orange band was eluted with CH_3OH (100 ml). The solvent was removed under reduced pressure. The residue was suspended in CH_2Cl_2 (20 ml) and the mixture was filtered. The solvent was removed from the mother liquor under reduced pressure giving an orange hygroscopic glassy residue of $[Et_4N]_2$**2** that was used without further purification. IR (Nujol, cm^{-1}): 1619 [ν(CO)amide], 1575 [ν(CO)amide], 1534 [ν(CO)amide]. Careful purification of an iron(III) starting material was more conveniently approached by dealing with the axial aqua monoanionic complex rather than this axial chloro dianionic complex. [Et4N]$_2$**2** (550 mg, ca. 0.7 mmol) was dissolved in CH_3CN (50 ml). Silver tetrafluoroborate (140 mg, 0.7 mmol) was dissolved in CH_3CN (2 ml) and was added to the solution which was stirred (1 h). The AgCl precipitate was filtered and the solvent was removed under reduced pressure. The resulting $[Et_4N]$**3** was further purified by elution through a silica gel column (8% MeOH in CH_2Cl_2). The solvent was removed under reduced pressure and the product was recrystallized from H_2O. Yield: 360 mg (~77%, variable solvation with water was found in different microcrystalline samples). IR (Nujol, cm^{-1}): 1590 [ν(CO)amide], 1565 [ν(CO)amide], 1535 [ν(CO)amide] $C_{29}H_{46}N_5FeO_5Cl_2 \cdot (H_2O)$ (689.5): calcd C 50.52, H 7.02, N 10.16, Cl 10.28; found C 50.24, H 6.84, N 9.82, Cl 10.32. ESI-MS (negative ion): *m/z* 522.2, $[\mathbf{3}\text{-}H_2O]^{1-}$ (100%); *m/z* 269.7, $[\mathbf{3}\text{-}H^+]^{2-}$ (18%).

5.5.2. Ce(IV) oxidation of the Fe(III) Cl complex by one electron

$[Et_4N]_2$**2** (500 mg, ca. 0.6 mmol) was dissolved in CH_2Cl_2 (30 ml). Ammonium cerium(IV) nitrate (10.3 g, 18.3 mmol) was added to the solution and the mixture was stirred (2 h). The solid cerium salts were removed by filtration. The purple product was obtained by removing the solvent under reduced pressure and drying under vacuum. Yield: 400 mg (~95%). Purple crystals were obtained by recrystallization from CH_2Cl_2–Et_2O. IR (Nujol, cm^{-1}): 1688 [ν(CO)amide], 1611 [ν(CO)amide],

1582 [ν(CO)amide]. ESI-MS (negative ion): *m/z* 557, $[\mathbf{4}]^{1-}$ (100%); *m/z* 522, $[\mathbf{4}\text{-Cl}]^{1-}$ (65%).

5.5.3. Synthesis of the pure Fe(IV) CN complex

$[Et_4N]\mathbf{4}$ (225 mg, 0.33 mmol) was suspended in H_2O (10 ml). Sodium cyanide (140 mg, 2.85 mmol) was dissolved in H_2O (10 ml) and added to the suspension and the mixture was sonicated (Branson 1200, 0.5 h). The purple suspension changed to a deep blue solution and nearly all the solid material dissolved. The mixture was filtered and the blue product was preciptated by adding $[PPh_4]Cl$ dissolved in water (600 mg, 1.6 mmol, 10 ml, Aldrich). The blue precipitate was collected and washed with H_2O (2 × 10 ml). Yield: 250 mg (0.28 mmole, ~85%). This material (120 mg) was further purified by TLC (Silica gel plate, GF, 20 × 20 cm × 1000 gm, 10:1 CH_2Cl_2–CH_3CN). The blue material was extracted from the silica gel with CH_3CN–CH_2Cl_2 (1:1, 60 ml). The solvent was removed under reduced pressure and the residue was dissolved in CH_2Cl_2 (3 ml) and filtered. Addition of pentane (150 ml) gave a blue powder (90 mg, 0.10 mmol), (Yield following purification: 75%). IR (Nujol, cm^{-1}): 2129 [ν(CN)], 1659 [ν(CO)amide], 1598 [ν(CO)amide], 1571 [ν(CO)amide]; $C_{46}H_{44}N_5FeOCl_2P$ (840.6): calcd C 62.18, H 4.99, N 7.88, Cl 7.98; found C 61.96, H 5.04, N 7.84, Cl 8.06. ESI-MS (negative ion): *m/z* 548.2, $[\mathbf{5}]^{1-}$ (100%); *m/z* 522.1, $[\mathbf{5}\text{-CN}]^{1-}$ (20%). For ^{13}C-labeled cyanide: *m/z* 549.2, $[\mathbf{5}]^{1-}$ (100%); *m/z* 522.1, $[\mathbf{5}-{}^{13}CN]^{1-}$ (8%).

5.5.4. Synthesis of a mixture of the Fe(IV) CN complex and the organic hydantoin

$[Et_4N]\mathbf{3}$ (160 mg, 0.23 mmol) was dissolved in the chosen nitrile solvent (6 ml). Base was added ($[Et_4N]OH$, 20 wt% in water, 0.370 ml, 0.52 mmol, Aldrich), then peroxide (*t*-BuO_2H, 90%, 0.605 ml, 5.4 mmol, Aldrich) was added dropwise with stirring (20 min) resulting in a blue solution. The volatiles were removed under reduced pressure, leaving an oily blue residue which was dissolved in H_2O (15 ml) and filtered. The blue material was precipitated from the filtrate by addition of an aqueous solution of $[PPh_4]Cl$ (800 mg, 2.1 mmol, Aldrich, 10 ml). The blue precipitate was collected and washed with H_2O (2 × 10 ml). Yield: 130 mg, 0.15 mmol (65%). Further purification was carried out as described in the $[Ph_4P]\mathbf{5a}$ section.

5.5.5. Synthesis of the pure organic hydantoin

$[Et_4N]_2\mathbf{2}$ (130 mg, 0.13 mmol) was dissolved in CH_3CN (5 ml, Aldrich). A 90% solution of *t*-butyl hydroperoxide (0.445 ml, 4 mmol, Aldrich) was added slowly (3 min). The reaction mixture was stirred (25 min) and then all liquids were removed under reduced pressure. The blue residue was dissolved in CH_2Cl_2 and loaded onto a preparative TLC plate (Silica gel GF, 1000 JAM, 20 cm × 20 cm) and developed with 15% CH_3CN in CH_2Cl_2. The product band was detected under UV irradiation at an R_f value of 0.3. Other product bands included the blue $[Et_4N]\mathbf{5}$, a brown-yellow species that remained at the origin, and two faint colorless bands present in less than 10% of the principal band at 0.3 R_f. The portion of the silica that contained the product was removed from the preparative plate and product was extracted with CH_2Cl_2–CH_3CN (1:1). The solution was filtered and the solvent was removed

under reduced pressure. A solid was obtained by dissolving the residue in CH_2Cl_2 (3 ml) followed by addition of pentane (150 ml). The solid was collected by filtration and was then washed with pentane (2 × 10 ml). Yield: 9 mg (14.8%) of pure 1-[2-((*E*)-2-butenyl-2-ethylamido)-2-methylpropanamido]-2-[5,5-dimethylhydantoin]-4,5-dichlorobenzene, **6**. IR (Nujol, cm^{-1}): 1780 [ν(CO)hydantoin], 1723 [ν(CO)hydantoin], 1665 [ν(CO)amide], 1631 [ν(CO)amide], 1582 [ν(CO)amide]. ^1H NMR (CD_3CN, δ ppm): 0.83 (*t*, 3H, $J=7$ Hz), 1.4 (*s*, 6H), 1.45 (*s*, 6H), 1.70 (*d*, 3H, $J=7$ Hz), 2.25 (*q*, 2H, $J=7$ Hz) 6.25 (*q*, 1H, $J=7$ Hz), 6.60 (*s*, 1H, NH) 6.70 (*s*, 1H, NH) 7.48 (*s*, 1H, ArH), 8.10 (*s*, 1H, ArH), 9.10 (*s*, 1H, NH); (CD_2Cl_2, δ ppm) δ:0.97 (*t*, 3H, $J=7$ Hz), 1.27 (*s*, 12H) 1.75 (*d*, 3H, $J=7$ Hz) 2.30 (*q*, 2H, $J=7$ Hz) 5.50 (*s*, 1H, NH) 6.00 (*s*, 1H, NH), 6.27 (*q*, 1H, $J=7$ Hz) 7.35 (*s*, 1H, ArH), 8.30 (*s*, 1H, ArH), 9.77 (*s*, 1H, NH). ^{13}C NMR (CD_2Cl_2, δ ppm): 13.4, 13.6, 20.2, 25.4, 30.0, 58.5, 59.6, 121.9, 125.2, 127.8, 129.7, 130.3, 133.8, 134.9, 139.2, 154.3, 170.5, 172.5, 175.9. For MS results, see below.

5.6. *X-ray crystal structure data and refinement for an Fe(III)(H_2O) complex*

(See Fig. 2) $C_{29}H_{48}Cl_2FeN_5O_6$, $M=689.47$, Triclinic, Space group P1, $a=9.899(2)$; $b=11.771(2)$; $c=14.991(4)$ Å, $\alpha=95.33(2)$; $\beta=100.09(2)$; $\gamma=92.31(2)°$, $V=1709.6(6)$ Å^3, $D_{obs}=1.33$ g cm^3, D_{calcd} ($Z=2$) $=1.339$ g cm^{-3}, $T=293$ K, $\lambda=0.71069$ Å, $\mu=0.64$ mm^{-1}, trans coeff. 0.87–1.00. Diffraction data were collected at room temperature on an Enraff–Nonius CAD-4 diffractometer using graphite monochromated *Mo*−*Kᾱ* radiation. Three reflections were monitored throughout data collection, only random fluctuations in intensity being observed. The structure was solved by direct methods[42]. Hydrogen atoms bonded to the carbon were included in calculated positions (C–H=0.96 Å) and were refined using a riding model with thermal parameter 20% greater than the parent carbon. Hydrogen atoms of the water molecule were located from electron density difference maps and their coordinates allowed to refine with the thermal parameter fixed at 20% greater than that of the oxygen. Refinement was by full-matrix least squares (Sheldrick, 1995 no. 72 [42]) on F^2 with scattering factors taken from the International Tables [43]. All non-hydrogen atoms were refined with anisotropic thermal parameters. The final difference maps were featureless. Refinement converged to $R=0.053$, w$R2=0.112$ with weights $1.0/[\sigma^2(F_o^2)+\{0.0652(F_o^2+2F_c^2)/3\}^2]$ for 2262 observed reflections.

5.7. *X-ray crystal structure data and refinement for the oxidized Fe(III)Cl complex*

(See Fig. 3) Single crystals of $[Et_4N]$**4** at 20 ± 1 °C are monoclinic, space group $P2_1/c-C_{2h}^5$ (no.14) with $a=9.958(2)$, $b=14.956(3)$ and $c=22.688(5)$ Å; $\alpha=90.00$, $\beta=93.83(2)$ and $\gamma=90.00°$; $V=3372(1)$ Å^3 and $Z=4$ ($d_{calcd}=1.357$ g cm^{-3}; $\mu_a(CuK\bar{\alpha})=6.17\ mm^{-1}$). A total of 4626 independent absorption-corrected reflections having $2\theta(CuK\bar{\alpha})<115.0°$ were collected using θ-2θ scans and Ni-filtered $CuK\bar{\alpha}$ radiation. The structure was solved using "direct methods" techniques with the Nicolet SHELXTL software package as modified at Crystalytics Company. The resulting structural parameters have been confined to a convergence of

R_1(unweighted, based on F)=0.037 for 2680 independent reflections having $2\theta(\mathrm{CuK}\bar{\alpha}) < 115.0°$ and $I > 3\sigma(I)$. The 10 methyl groups were refined as rigid rotors with sp^3-hybridized geometry and a C–H bond length of 0.96 Å. The initial orientation of each methyl group was determined from difference Fourier positions for the hydrogen atoms. The final orientation of each methyl group was determined by three rotational parameters. The refined positions for the rigid rotor methyl groups gave C–C–H angles which ranged from 103–118°. The remaining hydrogen atoms were included in the structure factor calculations as idealized atoms (assuming sp^2- or sp^3-hybridization of the carbon atoms and a C–H bond length of 0.96 Å) riding on their respective carbon atoms. The isotropic thermal parameter of each hydrogen atom was fixed at 1.2 times the equivalent isotropic thermal parameter of the carbon to which it is covalently bonded.

5.8. Mass spectrometric characterization of the organic hydantoin

It was possible to separate $[Et_4N]$**5** into two principal components: a colorless compound present in small quantities (< 10% of total mass), **6**, and a blue compound that was shown to be identical to the Fe^{IV}–CN product produced from the metathesis synthesis. On silica gel, **6** had an identical R_f value to $[PPh_4]$**5** over a range of developing conditions, which explained the initial difficulties experienced in our attempts to separate these oxidation components. ^1H and ^{13}C NMR spectra of **6** and of a form produced by deuteration of water-exchangeable protons revealed that **6** was diamagnetic and that it contained many of the functional groups of the macrocyclic tetraamide. However, ^1H NMR revealed new features including a quartet at 6.25 ppm which was shown to be coupled to a doublet at 1.70 ppm (J= 7 Hz), suggesting the presence of an olefinic CH coupled to a geminal CH_3 group. Thus, it appeared that this metal-free species had been produced by alteration of one of the two ethyl groups on the macrocyclic backbone. Initial characterization of **6** by FAB-MS indicated that the monoisotopic molecular mass was 468 Da, as evidenced by the moderately intense ions at m/z 469, 471 and 472, with the appropriate relative intensities for two chlorine atoms. Together with elemental analysis data, the NMR and FAB-MS data revealed that **6** was a metal-free species derived from the tetraamido-*N* ligand in which the ligand had undergone degradation at the six-membered ring. Two formulations fitted the data, namely, a dimethylhydantoin ring-containing product and an eleven-membered ring-containing product (Fig. 10). Since the NMR and FAB-MS data did not convincingly distinguish between the two possibilities, we sought to resolve all uncertainty about the formulation by using a combination of additional mass spectrometric techniques.

The base peak in the FAB mass spectrum was at m/z 182, and a significant ion at m/z 154 was also observed. When **6** was analysed by electron impact ionization (EI) mass spectrometry, a relatively weak molecular ion cluster (less than 1% of the base peak) at m/z 468/470/472 was detected, also with the appropriate pattern for two chlorine atoms. The base peak in the EI mass spectrum was at m/z 97. Chlorine-containing fragments roughly equal in intensity to the molecular ion were seen at m/z 411/413/415 and m/z 399/401/403, representing losses of 57 and 69 mass

units, respectively. Both of these fragments could be readily formed from either the hydantoin ring-containing product (Fig. 12) or the 11-membered ring species. Other significant fragments were observed at *m/z* 287/289/291 and *m/z* 154, with less intense signals found at *m/z* 182, 140, 84, 69 and 58.

Examination of the hydantoin ring containing structure revealed that single bond cleavages along the enediamide chain could produce the fragments with *m/z* values of 69, 97, 154 and 182. Formation of *m/z* 84, on the other hand, required cleavage across the hydantoin ring in conjunction with hydrogen migration. Inspection of the 11-membered ring containing product showed that it was also possible to generate the observed ions, although multiple bond cleavages would be required. While these latter cleavages are decidedly less favourable than the ones associated with the hydantoin ring containing structure, the 11-membered ring product could not be ruled out on the basis of the EI mass spectrum, alone. Further evaluations by tandem MS and accurate mass analysis in addition to deuterium exchange studies were, therefore, conducted. The results are summarized in Table 2. Although the results are consistent with the ion at *m/z* 140 being a product of *m/z* 154, generated by the loss of the elements of CH_2, we have not yet been able to devise a simple mechanism for the formation of this ion.

Deuterium exchange of susceptible hydrogens was accomplished by exposing **6** to D_2O. EI-MS revealed that the ion at *m/z* 58 was predominately shifted to *m/z* 59, with a small peak also seen at *m/z* 60. The ions at *m/z* 69 and *m/z* 84 remained unchanged, as did the base peak at *m/z* 97. On the other hand, more than 70% of the *m/z* 154 species shifted to *m/z* 155 as did the *m/z* 182 ion to *m/z* 183. The fragment corresponding to the ion at *m/z* 140 picked up either one or two deuterium atoms with equal frequency, consistent with the ion at *m/z* 140 being a product of *m/z* 154, generated by the loss of the elements of CH_2. These results suggested that the fragments represented by ions at *m/z* 58, 140, 154 and 182 contained a single exchangeable hydrogen. Tandem mass spectrometry and accurate mass analysis was then conducted on selected ions (Table 2). The results were consistent with the absence of an exchangeable hydrogen in the *m/z* 84 fragment and the presence of

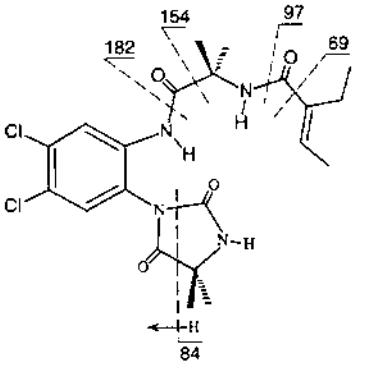

Fig. 12. Fragmentation pattern for the hydantoin ring-containing product.

Table 2
Accurate mass analysis, MS–MS analysis of **5b** and results following exposure of **5b** to D_2O

Ion (*m/z*)	Predicted high resolution mass		Found		Predicted exchangeable *H*[c]		Found	MS–MS analysis	
	11-Mem. ring compound	Hydantoin compound	Mass	Composition	11-Mem. ring compound	Hydantoin compound		Precursors (*m/z*)	Products (*m/z*)
58	58.0656	58.0656	58.0656	C_3H_8N	1	1	1	154,287	40,42,56,59
84	84.0449	84.0449	84.0447	C_4H_6NO	0 or 1	0 or 1	0	287	98,112,123
140	140.071[a]	140.1075	140.1083	$C_8H_{14}NO$	0	1	1 and 2	154	98,112,123
154	154.0741[b]	154.1231	154. 1217	$C_9H_{16}NO$	0	1	1	182	58,97
182	182.1180	182.1180	182. 1180	$C_{10}H_{16}NO_2$	0	1	1	468	69,97,154

[a]Predicted accurate mass value for ion which would include an exchangeable hydrogen. A fragment with a calculated mass of 140.1083 can be produced from the 11-membered ring structure, but it would not contain an exchangeable hydrogen.
[b]Analogously, the ion with a calculated mass of 154.1231 would not contain an exchangeable hydrogen.
[c]Based on EI-MS and EI-MS–MS.

one in the *m/z* 58 species. Information gained from the *m/z* 182 ion was totally consistent with the parent molecule being the hydantoin ring-containing product. Not only did the observed mass match the calculated value of 182.118, but the proposed structure would be expected to increase by 1 mass unit after exposure to D_2O. On the other hand, for the 11-membered ring product, an ion of identical molecular formula could be produced through a combination of C–C and C–N bond cleavages in conjunction with hydrogen transfer. However, that structure would not contain an amide hydrogen available for exchange. The ion at *m/z* 154 was equally informative. Both proposed products are able to fragment to an *m/z* 154 species capable of deuterium exchange. The expected mass for the fragment from the hydantoin ring-cqntaining product would be 154.1231, in close agreement with the observed value. However, the corresponding ion from the 11-membered ring structure would be 154.0741; this difference of 48 mmu from the observed result is beyond anticipated experimental error. Finally, the tandem MS and accurate mass experiments showed that the ion at *m/z* 140 was a product of *m/z* 154, through the loss of the elements of CH_2. Fragmentation of the *m/z* 154 species from the hydantoin ring-containing product leads to an ion with a calculated mass of 140.1075 with an exchangeable amide hydrogen, in agreement with observed results. In contrast, the *m/z* 140 ion that can be generated from the 11-membered ring fragment would have an ion mass of 140.0711 and no exchangeable amide. In concert, these results support the identity of **6** as the hydantoin ring-containing product and rule out the 11-membered ring structure.

Acknowledgements

This work was supported by the NIH, GM44867 (T.J.C.) and GM22701 (E.M.). We thank Professor Larry Que and Dr Anne True of the University of Minnesota for EXAFS analysis of **5** and Professor David Bocian for ascertaining that **5** rapidly photobleaches when studied by resonance Raman. We also thank Dr Colin Horwitz of Carnegie Mellon University for helpful discussions.

References

[1] T.J. McMurray, J.T. Groves, in: P.R. Ortiz de Montellano (Ed.), Cytochrome P-450. Structure, Mechanism and Biochemistry, Plenum Press, New York, 1986, pp. 1–28.
[2] P.R. Ortiz de Montellano, in: P.R. Ortiz de Montellano (Ed.), Cytochrome P-450. Structure, Mechanism and Biochemistry, Plenum Press, New York, 1986, pp. 217–271.
[3] J.D. Lipscomb, Ann. Rev. Microbiol. 48 (1994) 371.
[4] A.L. Feig, S.J. Lippard, Chem. Rev. 94 (1994) 759–805.
[5] A.C. Rosenzweig, S.J. Lippard, Acc. Chem. Res. 27 (1994) 229–236.
[6] L. Que, Jr, in: J. Reedijk (Ed.), Bioinorganic Catalysis, Dekker, New York, 1993, pp. 347–393.
[7] R.H. Holm, Chem. Rev. 87 (1987) 1401–1449.
[8] R.S. Drago, Coord. Chem. Rev. 117 (1992) 185–213.
[9] C.L. Hill (Ed.), Activation and Functionalization of Alkanes. Vol. 0, Wiley, New York, 1989.

[10] D.H.R. Barton, A.E. Martell, D.T. Sawyer (Eds.), The Activation of Dioxygen and Homogeneous Catalytic Oxidation, Vol. 0, Plenum Press, New York, 1993.
[11] L.I. Simandi, Catalytic Activation of Dioxygen by Metal Complexes, Kluwer Academic Publishers, Dordrecht, 1992.
[12] R.A. Sheldon, J.K. Kochi, Metal Catalyzed Oxidations of Organic Compounds, Academic Press, New York, 1981.
[13] I.W.C.E. Arends, K.U. Ingold, D.D.M. Wayner, J. Am. Chem. Soc. 117 (1995) 4710–4711.
[14] J. Kim, R.G. Harrison, C. Khim, L. Que Jr., J. Am. Chem. Soc. 118 (1996) 4373–4379.
[15] T. Kojima, R.A. Leising, S. Yan, L. Que Jr., J. Am. Chem. Soc. 115 (1993) 11328–11335.
[16] R.A. Leising, R.E. Norman, QueL., Jr, Inorg. Chem. 29 (1990) 2553–2555.
[17] R. A. Leising, Y. Zang, L. Que Jr, J. Am. Chem. Soc. 1991 (1991) 8555–8557.
[18] R.A. Leising, J. Kim, M.A. Pérez, L. Que Jr., J. Am. Chem. Soc. 115 (1993) 9524–9530.
[19] T.J. Collins, Acc. Chem. Res. 27 (1994) 279–285.
[20] M.J. Bartos, C. Kidwell, K.E. Kauffmann, S.W. Gordon-Wylie, T.J. Collins, G.C. Clark, E. Münck, S.T. Weintraub, Angew. Chem. Int. Edn. Engl. 34 (1995) 1216–1219.
[21] K.L. Kostka, B.G. Fox, M.P. Hendrich, T.J. Collins, C.E.F. Rickard, L.J. Wright, E. Münck, J. Am. Chem. Soc. 115 (1993) 6746–6757.
[22] T.J. Collins, B.G. Fox, Z.G. Hu, K.L. Kostka, E. Münck, C.E.F. Rickard, L.J. Wright, J. Am. Chem. Soc. 114 (1992) 8724–8725.
[23] T.J. Collins, R.D. Powell, C. Slebodnick, E.S. Uffelman, J. Am. Chem. Soc. 112 (1990) 899–901.
[24] J.M. Wotkman, R.D. Powell, A. Procyk, T.J. Collins, D.F. Bocian, Inorg. Chem. 31 (1992) 1548–1550.
[25] T.J. Collins, S. Gordon-Wylie, J. Am. Chem. Soc. 111 (1989) 4511–4513.
[26] F.M. MacDonnell, N.L.P. Fackler, C. Stem, T.V. O'Halloran, J. Am. Chem. Soc. 116 (1994) 7431–7432.
[27] F.C. Anson, T.J. Collins, T.G. Richmond, B.D. Santarsiero, J.E. Toth, B.G.R.T. Treco, J. Am. Chem. Soc. 109 (1987) 2974–2979.
[28] U. Knof, T. Weyhermuller, T. Wolter, K. Wieghardt, E. Bill, C. Butzlaff, A.X. Trautwein, Angew. Chem. Int. Ed. Engl. 32 (1993) 1635–1638.
[29] G.P. Gupta, G. Lang, W.R. Scheidt, D.K. Geiger, C.A. Reed, J. Chem. Phys. 85 (1986) 5212–5220.
[30] G.P. Gupta, G. Lang, C.A. Reed, K. Shelly, W.R. Scheidt, J. Chem. Phys. 86 (1987) 5288–5293.
[31] N.N. Greenwood, T.C. Gibb, Mössbauer Spectroscopy, Chapman and Hall, London, 1971.
[32] M.J. Bartos, C. Kidwell, K.E. Kauffmann, S.W. Gordon-Wylie, T.J. Collins, G.C. Clark, E. Münck, S.T. Weintraub, Angew. Chem. Int. Edn. Engl. 34 (1995) 1216-1219.
[33] G.P. Gupta, G. Lang, C.A. Reed, K. Shelly, W.R. Scheidt, J. Chem. Phys. 86 (1987) 5288–5293.
[34] W.T. Oosterhuis, G. Lang, J. Chem. Phys. 58 (1973) 4757–4765.
[35] C.C. Cummins, R.R. Schrock, Inorg. Chem. 33 (1994) 395–396.
[36] O.M. Reinauld, Theoplod, K. H. J. Am. Chem. Soc. 116 (1994) 6979–6980.
[37] S. Mahapatra, J.A. Halfen, E.C. Wilkinson, QueL., Jr, W.B. Tolman, J. Am. Chem. Soc. 116 (1994) 9785-9786.
[38] D.M. Golden, S.W. Benson, Chem. Rev. 69 (1969) 125.
[39] C.P. Horwitz, D.R. Fooksman, L.D. Vuocolo, S.W. Gordon-Wylie, N.J. Cox, T.J. Collins, J. Am. Chem. Soc.
[40] T.J. Collins, C. Slebodnick, E.S. Uffelman, Inorg. Chem. 29 (1990) 3433–3436.
[41] T.J. Collins, R.D. Powell, C. Slebodnick, E.S. Uffelman, J. Am. Chem. Soc. 113 (1991) 8419–8425.
[42] G.M. Sheldrick, Acta Crystallogr. A46 (1990) 467.
[43] International Tables for Crystallography, Kluwer Academic, Dordrecht, 1992.